Planetary and Space Science 57 (2009) 1076–1084

Contents lists available at ScienceDirect

Planetary and Space Science

journal homepage: www.elsevier.com/locate/pss

A preparatory study on subsurface exploration on Mars using GPR and microwave tomography

Francesco Soldovieri [a,*], Giancarlo Prisco [a], Svein-Erik Hamran [b,1]

[a] Istituto per il Rilevamento Elettromagnetico dell'Ambiente, Consiglio Nazionale delle Ricerche Via Diocleziano 328, 80124 Napoli, Italy
[b] Forsvarets Forsknings Institutt-FFI, P.O. Box 25, 2007 Kjeller, Norway

ARTICLE INFO

Article history:
Received 3 April 2008
Received in revised form
20 September 2008
Accepted 25 November 2008
Available online 7 December 2008

Keywords:
Ground penetrating radar (GPR)
Subsurface prospection
Microwave tomography

ABSTRACT

The exploitation of ground penetrating radar in Mars subsurface exploration is becoming assessed in remote sensing observations and is of timely interest for high resolution in situ prospecting of the first meters of the underground.

In this framework, we deal with a novel processing approach based on microwave tomography. Aiming to achieve accurate and reliable "images" of the investigated subsurface region in order to detect, localize and possibly determine the extent and the geometrical features of the embedded layers while reducing at the minimum possible the "interpretation" of the diagnostics result.

The feasibility of the microwave tomographic approach has been tested in realistic cases dealing with conditions analogue to the Mars subsurface ones. In particular, we will present the tomographic reconstruction results achieved by experimental data collected in a field survey at Svalbard Islands (Norway) with a time-domain GPR.

1. Introduction

In the Mars exploration, a significant activity has been made in the previous years with the aim of detecting the subsurface liquid water and life signs.

First measurements performed by the Mars Odyssey spacecraft revealed the presence of a large amount of hydrogen in the top tens of cm below the surface in polar and high-latitude regions and south of 50–60° (Feldman et al., 2002; Mitrofanov et al., 2002). The hydrogen observed by the instruments is generally interpreted as the signature of large subsurface ice deposits. Differently, at mid-latitudes, it has been hypothesized that ice should be accumulated from atmospheric water vapour under a thin regolith blanket whose depth is governed by the frost temperature level and the surface material porosity (Paige, 1992). The icy layer accumulated from deposited atmospheric water should therefore be found at greater depths at lower latitudes.

Furthermore, models of the thermal structure of Mars crust have suggested that that the thickness of frozen ground (the depth at which the local temperature rises above the ice fusion point) range from 2.5–5.0 km at the equator to 6–12 km at the poles (Clifford, 1993; Clifford and Parker, 2001).

On the other hand, observations of the surface of Mars have given indications of features similar to those created by ice and water erosion, leading to a belief that at one point in time Mars may have had rivers, lakes, glaciers, and possibly even an atmosphere comparable to that found on the Earth. There is an evidence that Mars had and still may contain a significant amount of water within its surface in the form of permafrost, ice, or liquid water. In this framework, one of the most obvious indicators for the past existence of water on Mars' surface are channels. By analyzing this onset diameter of rampart craters, it has been hypothesized that the depth of ice on Mars may range from 100 m at around 50° latitude to 300–400 m at the equator.

Images from the Mars Orbiter camera (MOC) aboard the Mars Global Surveyor (MGS) have helped to reinforce this belief (Leuschen et al., 2003a, b; Malin and Edgett, 2000). Water could flow out from an underground ice rich saturated layer covered locally by volcanic altered materials (Malin and Edgett, 2000). Moreover, these observations have opened up a broad discussion of whether water or liquid CO_2 aquifers caused these features.

The existence of CO_2 ice on the surface of Mars was hypothesized almost 40 years ago (Leighton and Murray, 1966) and has been proven by Mariner 9 and Viking observations. The detection of solid CO_2 at surface, on the polar caps as well as in other regions, and in the subsurface (within the regolith) of Mars is therefore fundamental to validate or refute such new hypotheses.

Therefore, the investigation of the Martian polar caps and their layered structure are thought to hold crucial information on the

* Corresponding author. Tel.: +39 081 5704945, +39 081 5707999; fax: +39 5705734.
E-mail addresses: soldovieri.f@irea.cnr.it (F. Soldovieri), svein-erik.hamran@ffi.no (S.-E. Hamran).
[1] Tel.: +47 63 80 72 54.

0032-0633/$ - see front matter © 2008 Elsevier Ltd. All rights reserved.
doi:10.1016/j.pss.2008.11.014

climatic history and the hydrologic cycle of Mars. In particular, the necessity arises to give answer to the crucial questions about the composition of the caps as due to water ice, or are other phases such as silicate inclusions, dry ice, and CO_2-clatherates significant components. Most of what is known about the caps derives from remote sensing of their upper few meters and observations of their surface, troughs, and scarps.

Ground penetrating radar (Leuschen et al., 2003a, b) in contrast has the capability of providing a three-dimensional (3D) view of the polar caps because H_2O and CO_2 ices possess very low electric conductivity and, consequently, only weakly attenuate the propagation of electromagnetic (EM) waves. Mixtures of these ices with generic impurities such as sediment and salts have a wide range in permittivity and conductivity values. It is exactly these variations in material electrical properties that a radar sounder might detect in the subsurface, giving us the opportunity of mapping the layered structure of the Martian polar caps, perhaps the presence of melt water, and the interface between the polar deposits and the underlying crust.

The possibility to exploit the ground penetrating radar (GPR) in Mars subsurface exploration has been already demonstrated; thanks to remote sensing observations with low frequency radars (some MHz) allocated on satellite platforms (Plaut et al., 2007; Picardi et al., 2007; Alberti et al., 2007; Safaeinili et al., 2007) when the aim is to sound the deeper layers of the Marsis subsurface. In this framework, a significant role is played by the research activities concerned with the electromagnetic characterization of the Mars constitutive parameters since they affect the investigation depth and spatial resolutions limits achievable in GPR investigations; such a characterization activity has been performed via numerical analysis and by laboratory measurements on Martian soil analogues (Cerreti et al., 2007; Pettinelli et al., 2003).

For in situ-exploration, the development of high-frequency (from hundred of MHz to some GHz) GPR systems to be located on a rover platform is becoming of timely and significant interest (Hamran et al., 2007a, b, 2008); in this case the objective is to achieve a high-resolution investigation of the first meters of the subsurface. The results of such a high-resolution GPR prospection are of interest for many tasks such as: the characterization of shallower geological structures (stratifications); the detection and localization of individual scatterers; the comparison between the GPR measurements and drill sample; and the support to drill operations (choice of the optimal site and prevention of dangerous situations).

Very recently, the EISS experiment has been proposed with the aim of providing information on the structure and stratigraphy of the underground from the depth of several tens of meters to more than 1 km and with a horizontal resolution of the order of some hundred of meters (Ciarletti et al., 2007). The system exploits the combination of a fixed lander, the Geophysics Environmental Package (GEP), radiating in the HF frequency range and a receiver allocated on the ExoMars rover. The simultaneous presence of the rover and of the GEP allows to acquire data in a multi-monostatic configuration (due to the transmitting and receiving antennas on GEP) and under a multi-bistatic configuration thanks to the receiver allocated on the rover; for this latter configuration, the aim is to achieve a 2D image of the subsurface over the section made up of the depth and of the movement direction of the rover.

Many advantages push to consider GPR as one of the most suitable options for the rover package instrumentation such as: the possibility of non-invasive and fast measurement survey, the extreme versatility, the simplicity of use and the portability (Ori and Ogliani, 1996), the possibility to be integrated with other geophysical techniques such as ERT, EMI, TDEM (Vannaroni et al., 2004; Clifford et al., 2007).

GPR is based on radar principles (Daniels, 2004; Ori and Ogliani, 1996) and, in its simplest and most common configuration, is made up of a transmitting antenna, which radiates wideband radio-frequency pulses towards the air/soil interface, and of a receiving antenna which collects the electromagnetic signals backscattered by the buried targets. When the radiated wave impinges some discontinuity in the electromagnetic properties of the subsurface (representative of hidden layers, inhomogeneities), the radiated pulse is reflected, collected by the receiving antenna and finally represented to give information (in particular, the existence and location) about the targets.

For Mars subsurface exploration, the configuration of interest for rover GPR allocation is the monostatic where the receiving and transmitting antennas are physically separated by a fixed offset that is small in terms of the radiated wavelength. The antenna system is moved very close to or in contact with the air/ground interface. A time-domain trace is collected for each antenna's position, then the traces are joined to achieve a 2D raw data representation of the subsurface region. Usually, the raw data are worked out with signal processing based techniques in order to achieve the processed radargram. Finally, such a radargram is "interpreted" on the basis of the operator's expertise and on the priori information about the investigated scene with the final aim of obtaining information about the existence and location of the buried targets (Daniels, 2004).

In the recent years, novel processing approaches based on microwave tomography have been developed and exploited for GPR subsurface prospecting (Leone and Soldovieri, 2003; Soldovieri et al., 2007). These approaches account for explicitly the model of the electromagnetic scattering and formulate the reconstruction problem as an inverse one (Leone and Soldovieri, 2003). The aim is to provide accurate and reliable "images" of the investigated subsurface region in order to detect, localize and possibly determine the extent and the geometrical features of the embedded objects.

Here, we deal with a reconstruction approach based on a linear model of the electromagnetic scattering that results very convenient for practical and theoretical reasons. First, linear inversion algorithms are numerically efficient thus allowing to investigate domains large (in terms of the probing wavelength) in a quasi real-time also when a 3D representation of the scene is needed (Solimene et al., 2007). In addition, linear models permit to achieve the robustness of the solution algorithms with respect to the uncertainties in the parameters of the measurement configuration and on the investigated scenario (Persico and Soldovieri, 2004).

Turning to a theoretical point of view, the linear models allow further advantages such as: the absence of the false solutions (a question to be arisen when an inverse scattering problem faced without any approximation); the exploitation of well assessed regularization tools for achieving a stable solution of the problem (Bertero and Boccacci, 1998); the possibility to analyze and foresee the reconstruction performances of the algorithm once the measurement configuration and the properties of the reference scenario are known (Persico et al., 2005).

The microwave tomographic approach has been largely presented in many papers, some of them by the authors. The main aim of this paper is to present the features of the microwave tomography-based approach in the applicative framework of the MARS Exploration via GPR. In particular, this task is performed thanks to a preparatory study of the linear microwave tomographic approach for the characterization of the shallower layers of the Mars underground.

After the description of the microwave tomographic approach, we will turn to the main technical aim of the paper concerned with the experimental validation of the microwave tomographic approach in some realistic cases resembling the Mars subsurface conditions.

In particular, we will present the reconstruction results achieved by the experimental data collected in a field survey in front of the Uversbreen glacier located in Svalbard Islands, Norway, (latitude 78°50′, longitude 12°). Svalbard, meaning "cold coast," is an archipelago composed of four main islands and about 150 smaller ones. It is a Norwegian territory located about halfway between Tromso in Norway and the North Pole. Roughly 60% of Svalbard is glacierized and shaped by volcanism, ice, and liquid water, thus being similar to how Mars might have once been. Therefore, the Svalbard Islands were chosen as site of the the Arctic Mars Analog Svalbard Expedition (AMASE) (Steele et al., 2007).

The objective of the AMASE is to study an extreme Mars-like environment using instruments and techniques that may be used for future planetary missions.

In particular GPR survey was aimed to sounding low loss permafrost in order to give the reconstruction of the geometry of the interfaces between ice layer and sediment layers (more details will be given in the section about the experimental data). In particular, the microwave tomographic approach has been applied to measurements carried out by a time-domain GPR equipped with two antennas at 500 and 800 MHz, respectively (Hamran et al., 2007b).

Therefore, the paper is organised as follows. Section 2 is devoted to present briefly the solution algorithm and numerical results with the aim to pointing out the reconstruction capabilities of the approach. Section 3 is devoted to present the experimental validation of the microwave tomographic approach with data collected during the measurement survey at Uversbreen site. Finally, conclusions follow.

2. The microwave tomography-based approach

This section is devoted to give a brief description of a microwave tomographic approach based on the Born approximation (BA) of the electromagnetic scattering (Slaney et al., 1984; Leone and Soldovieri, 2003; Meincke, 2001; Persico et al., 2005).

BA is useful when penetrable objects are under investigation, as in the cases of interest for this paper where the attention is mainly focussed on buried layers detection and localization.

BA was originally developed to solve the forward problem, i.e., the determination of the field scattered from a known object under the incidence of a known electromagnetic field. Under BA, the electromagnetic field inside the object is approximated with the one when the object is absent (Slaney et al., 1984). Therefore, BA provides very accurate results for the scattered field when the hypothesis of weak scatterer holds, i.e., when an object whose dielectric permittivity is slightly different from one of the host medium and whose extent is small in terms of probing wavelength is considered (Slaney et al., 1984).

When an inverse scattering problem is tackled, the hypothesis of a weak scatterer can be relaxed at the cost to renounce to the "quantitative" reconstruction of the electromagnetic properties (dielectric permittivity and conductivity) of the object. Anyway, the adoption of a Born model inversion scheme allows to detect, to localize and to determine the geometry of the object also in the case of strong scattering objects; this has been shown by a large number of numerical and realistic experiments (Meincke, 2001; Soldovieri et al., 2007).

Compared to the classical migration technique (Stolt, 1978), microwave tomographic approach offers interesting advantages. In fact, it has been how the microwave tomographic approach has better performances in giving focused images of localized objects (Pettinelli et al., 2008); these better performances arise since the microwave tomographic algorithm is based on a more accurate model of the electromagnetic scattering. In addition, the approach here presented is able to counteract the effect of the noise on data thanks to well assessed regularization schemes and to give stable images of the investigated scene also in the presence of low signal to noise ratios.

Let us turn now to briefly present the microwave tomographic approach for the 2D geometry of interest for this paper.

The geometry of the problem is depicted in Fig. 1 and is concerned with the half-space scenario made up of two half-spaces (air and soil) separated by a planar interface at $z=0$. The upper half-space is air with a dielectric permittivity ε_0. The lower half-space has a *relative* dielectric permittivity ε_b and an electrical conductivity σ_b. The magnetic permeability is the same everywhere and is equal to μ_0, i.e., one of the free-space.

The incident field source is a time-harmonic (time dependence $exp(j2\pi ft)$) filamentary y-directed electric current, of non finite extent and invariant along the y-axis; such a source radiates in the frequency band ($f_{\min}$, $f_{\max}$) (multi-frequency configuration). As said above, the multi-monostatic measurement configuration is assumed, where the locations of the transmitting and receiving antennas coincide. In particular, the scattered field data are collected over a rectilinear observation domain at the air–soil interface ranging from $-x_M$ to x_M (see Fig. 1).

The relevant targets are invariant along the y-axis and their cross-section is enclosed in the rectangular investigation domain $D=(-a,a)X(z_{\min},z_{\max}+2b)$ (see Fig. 1).

We assume the relative dielectric permittivity $\varepsilon_r(x,z)$ and the conductivity $\sigma(x,z)$ distributions inside the investigation domain D as unknowns of the problem. Accordingly, the inverse problem is recast (Persico et al., 2005; Meincke, 2001; Leone and Soldovieri, 2003) in terms of the unknown contrast function, defined as

$$\chi(x',z')=\frac{\varepsilon_{eq}(x',z')-\varepsilon_{eqb}}{\varepsilon_{eqb}}, \qquad (1)$$

where $\varepsilon_{eq}\ (x',z')=\varepsilon_0\varepsilon_r(x',z')-j(\sigma(x',z')/2\pi f)$ and $\varepsilon_{eqb}=\varepsilon_0\varepsilon_b-j(\sigma_b/2\pi f)$ are the equivalent complex dielectric permittivity of the targets and of the soil, respectively. Therefore, the contrast function accounts for the relative difference between the unknown equivalent dielectric permittivity of the objects and one of the host medium (i.e., the soil).

Under the BA, the relationship between the unknown contrast function and the scattered field data is provided by the following

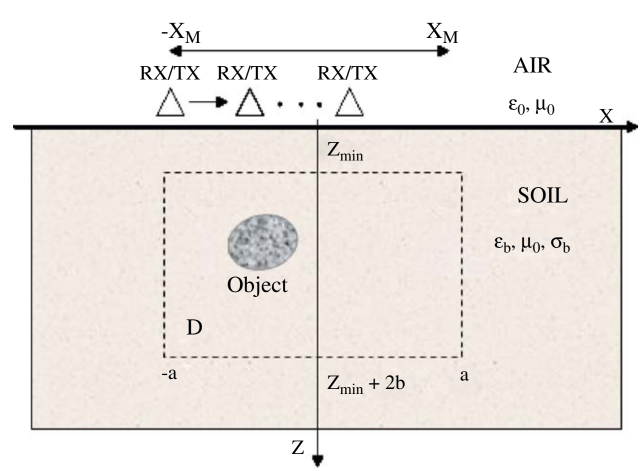

Fig. 1. Geometry of the problem.

linear integral equation *in the frequency domain* (Persico et al., 2005; Meincke, 2001; Leone and Soldovieri, 2003):

$$E_s(x_s,f) = k_s^2 \int_D G_e(x_s,f,\vec{r}')E_{inc}(x_s,f,\vec{r}')\chi(\vec{r}')d\vec{r}'$$
$$-x_M \leqslant x_s \leqslant x_M, f_{\min} \leqslant f \leqslant f_{\max}, \quad (2)$$

where f is the working frequency; x_s is the generic observation point and $k_s = 2\pi f\sqrt{\varepsilon_{eqb}\mu_0}$ is the wave-number in the soil.

$E_s(x_s,f)$ is the electric scattered field along the air–soil interface collected at the abscissa x_s and at the frequency f. In particular, as by its definition, the scattered field E_s is given as the 'difference' between the total field and the unperturbed field. The total field is measured in the presence of the buried objects and arises for two contributions: the field reflected at the interface air/soil and the field backscattered by the buried objects. The unperturbed field coincides with the field reflected by the interface air/soil when the objects are absent; therefore, the unperturbed field accounts for electromagnetic reflection/transmission phenomenon at the air/soil interface.

The kernel of the integral equation in Eq. (2) is given as the product of two functions: the Green's function $G_e(x_s,f,\vec{r}')$ and the incident field E_{inc}.

The Green's function $G_e(x_s,f,\vec{r}')$ represents the electric field generated at the observation point x_s by the elementary source located at the generic point $\vec{r}'$ in the soil. E_{inc} is the incident field, i.e., the electric field in the buried investigation domain D when the scattering objects are absent. Both the quantities are known once one has defined the reference scenario and the measurement configuration; for a more thorough understanding of their meaning and their expression the reader can refer to Leone and Soldovieri (2003).

The numerical implementation of the solution algorithm require the discretization of Eq. (2); this task is pursued by resorting to the method-of-moments (MoM) (Harrington, 1961). In particular, the linear integral relationship in Eq. (2) is discretized into a linear algebraic system where the unknown parameters are the expansion coefficients of the contrast function along the chosen functional basis and a point-matching is adopted in the data space (Leone and Soldovieri, 2003). The inversion of the resulting matrix is performed by a scheme based on the truncated Singular Value Decomposition (TSVD) (Bertero and Boccacci, 1998) able to give a good robustness of the solution algorithm with respect to the uncertainties and the noise on data; for more details, the interested reader is referred to Soldovieri et al. (2007) and references therein.

The reconstruction results will be given as the spatial map of the modulus of retrieved contrast function in Eq. (1); the regions, where the modulus of the contrast function is significantly different from zero, provide information about the location and the "geometry" of the buried objects. Therefore, when we refer to the tomographic reconstruction result, we mean the modulus of the retrieved contrast function $\chi(x',z')$ normalized with respect to its maximum.

Let us turn now to present some preliminary reconstruction results achieved by synthetic data. This analysis has two objectives. The first one is to outline the features of the reconstructed tomographic images with the objective of simplifying the interpretation of the experimental results that will be presented in the following section. The second one is concerned with the presentation of a pre-processing strategy that allows to pass from raw data in time-domain (as even occurs in the experimental case) to the suitable inversion data in the frequency domain.

Here, the synthetic data in the time-domain have been simulated by means of the GprMax 2D code (Giannopoulos, 2003) that exploits the finite-difference-time-domain (FDTD) method. Therefore, output of the FDTD simulation is the total field in the time-domain. As said above, such a field arises as due to two quantities: the field reflected by the interface air/soil and the field backscattered by the buried objects.

Now, the question arises to obtain the scattered field data in the frequency domain starting from the total field in the time-domain; this task is accomplished by a two-step procedure. The first step consists in "gating" the first part of all the time-domain traces; this operation provides an estimation of the time-domain scattered field. The second step consists in Fourier transforming the time-domain scattered field so to achieve data in a suitable form (frequency domain) for the inversion algorithm.

The chain of the overall combined pre-processing and inversion strategy is pictorially sketched in Fig. 2.

Let us now turn to present the reconstruction results with the synthetic data.

The first test case refers to the geometry of Fig. 3 with the buried interface between two different layers. The parameters adopted in the inversion and the properties of the two layers are listed in Table 1.

It is worth noting that the case at hand is concerned with a buried soil/water interface that is not very realistic for Martian shallow subsurface. Anyway, in this case the very different dielectric permittivity between the layers arises a strong reflection; therefore, this case aims to showing how the BA based inversion scheme works in presence of a strong scatterer.

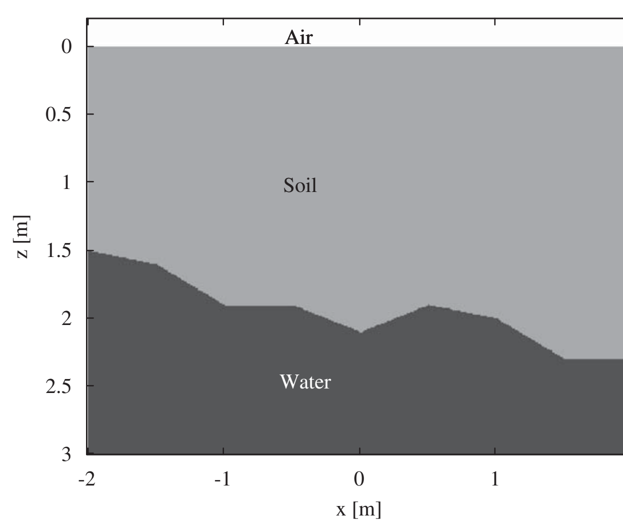

Fig. 3. 2D geometry of the problem for the first synthetic test case. A buried interface between the soil and a water layer is present.

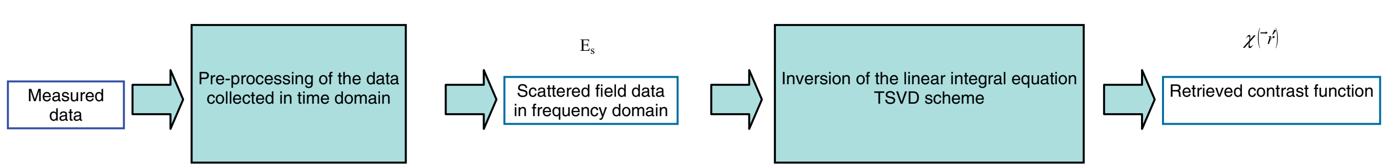

Fig. 2. Pictorial sketch of the combined pre-processing and inversion strategy.

Table 1
Parameters for the first synthetic case.

Parameter	Value
Model relative dielectric permittivity of the soil	4
Relative dielectric permittivity of the water	80
Model conductivity of the soil	0.005 S/m
Conductivity of the water	0.5 S/m
Spatial step of the measurements	0.05 m
Measurement domain	2 m (41 points spaced by 0.05 m)
Frequency band	100–1000 MHz
Frequency step	20 MHz (46 freq. exploited in the inversion)
Investigation domain	4 m (horizontal) × (1–3) m depth

Table 2
Parameters for the second synthetic case.

Parameter	Value
Model relative dielectric permittivity of the frozen sediment	5.76
Relative dielectric permittivity of the ice	3.15
Model conductivity of the frozen sediment	0.001 S/m
Conductivity of the ice	0.01 S/m
Spatial step of the measurements	0.05 m
Measurement domain	2 m (41 points spaced by 0.05 m)
Frequency band	100–1000 MHz
Frequency step	20 MHz (46 freq. exploited in the inversion)
Investigation domain	4 m (horizontal) × (1–3) m depth

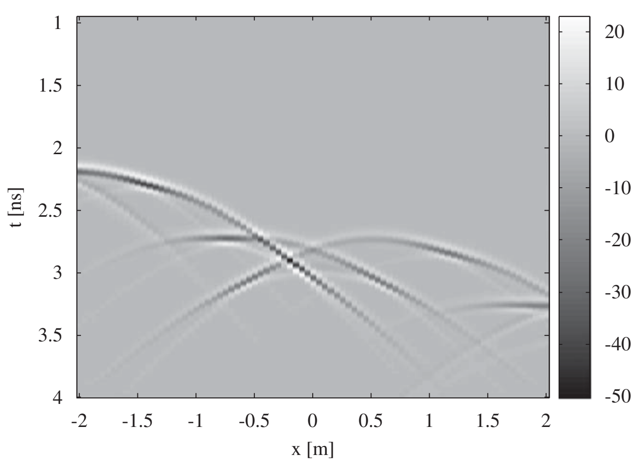

Fig. 4. Scattered field data in time-domain for the test case of Fig. 3. The contribution of the interface air/soil has been erased by a gating procedure.

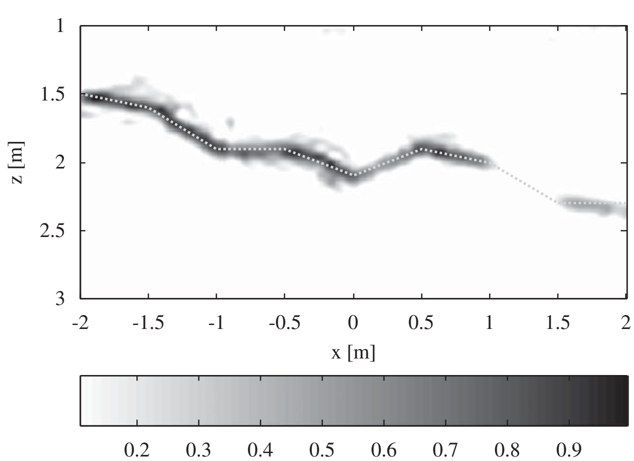

Fig. 5. Tomographic reconstruction for the test case of Fig. 3. The normalized modulus of the contrast function permits to point out the location and the shape of the buried interface.

Also, this case permits to point out in a simpler way the features of the tomographic reconstruction.

The time-domain scattered field data is presented in Fig. 4; by examining such a data, the geometry of the interface is not clearly "visible" and is represented mostly by hyperbolic curves. Conversely, the tomographic reconstruction result, i.e., the normalized modulus of the contrast function presented in Fig. 5, allows to clearly point out the geometry of the buried interface. We observe from Fig. 5 that the zone of the interface within the range 1–1.5 m is not retrieved in the tomographic image; however, this is not due to a limitation of the inversion approach but to the fact that, due to the position and orientation of this part of the buried interface, the relevant scattered field data is not collected over the chosen measurement domain.

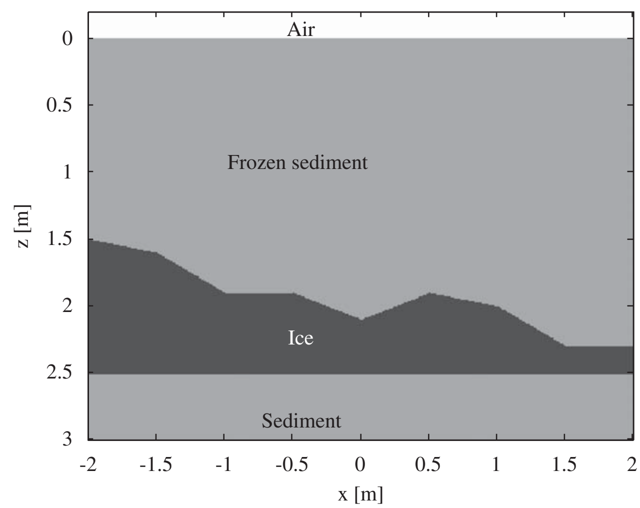

Fig. 6. 2D geometry of the problem for the second synthetic test case. A buried layer of ice is embedded in the frozen sediment.

The second test case is concerned with a more realistic scenario similar to the one considered in the section below for the experimental data. In particular, the parameters of the scenario, of the measurement configuration and of the inversion procedure as well as the properties of the layers are reported in Table 2. The aim of the reconstruction procedure was the localization and the shape reconstruction of the interfaces of a ice layer embedded in a sedimentary soil (see the geometry in Fig. 6). Figs. 7 and 8 depict the time-domain scattered field data and the tomographic reconstruction, respectively.

The tomographic reconstruction permits to localize and outline the geometry of the shallower (non-flat) interface with a good accuracy. Also the deeper (flat) interface is detected and its geometry is well reconstructed; however, we observe a delocalization of the deeper interface, this effect can be explained by stating that the electromagnetic velocity assumed in the Born model, approximately equal to $v_{model} = c_0/\sqrt{5.76} = 3{*}10^8/2.4 = 12.5\,\mathrm{cm/ns}$, is different from the actual one in the ice layer that is equal to $v_{ice} = c_0/\sqrt{3.15} = 3{*}10^8/1.77 = 16.9\,\mathrm{cm/ns}$. Therefore, the inversion approach, based on

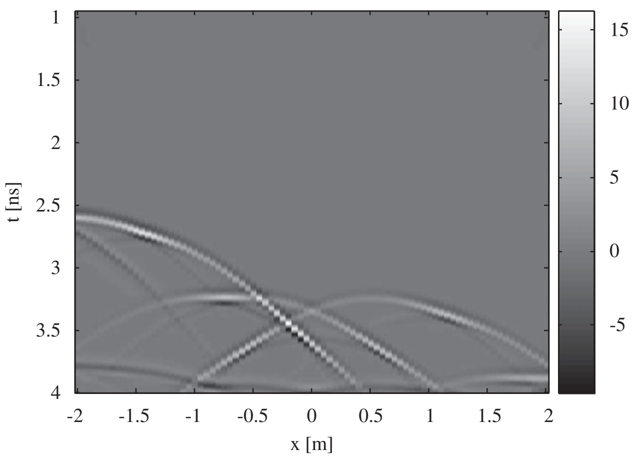

Fig. 7. Scattered field data in time-domain for the test case of Fig. 6. The contribution of the interface air/soil has been erased by a gating procedure.

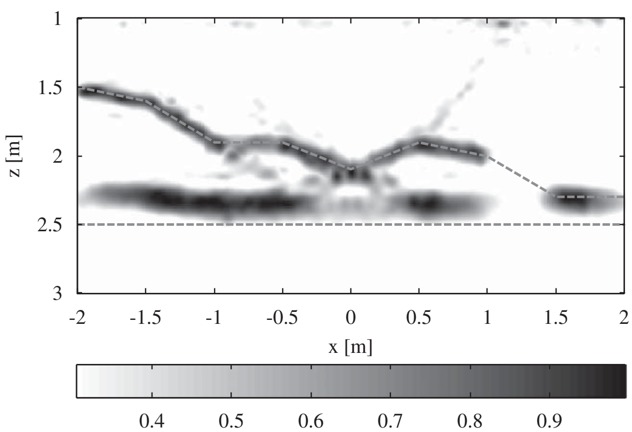

Fig. 8. Tomographic reconstruction for the test case of Fig. 6. The normalized modulus of the contrast function permits to point out the location and the shape of shallower and deeper interfaces of the ice layer.

the v_{model}, interprets the electromagnetic propagation in the ice layer with an electromagnetic velocity smaller than the actual one (v_{ice}); this leads to the reconstruction of the deeper interface at a smaller depth compared to the true position.

3. The experimental cases

This section is concerned with the processing of the data relative to the field survey in front of the two glaciers at Svalbard Islands, Norway.

GPR survey was performed in front of Comfortlessbreen and Uversbreen glaciers with the aim of demonstrating that GPR is a useful tool for detecting and mapping buried ice and ice pockets within permafrost sediments. Old aerial photographs 1936–1990 are used to show the origin of an isolated, sediment covered ice body, and illustrate how it has been buried. Together with a newly exposed ice/sediment cliff, this serves as excellent ground truthing for the GPR data.

The GPR wavelet phase polarities agreed with the observations and the electromagnetic wave velocities calculated from diffractions (0.115–0.135 m/ns for the sediment and 0.15–0.17 m/ns for the ice). In addition, GPR frequency dependent relations were established to quantify the loss of the signal power through the layer of sediment. In particular, it was pointed out that the loss

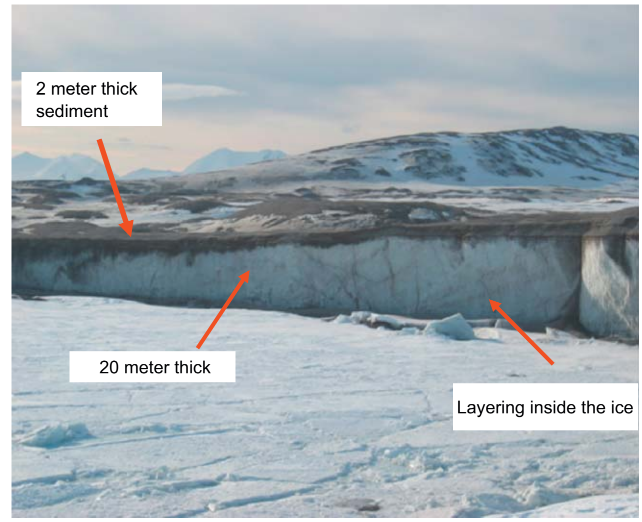

Fig. 9. The investigated scenario.

through ice was very low and the maximum penetration possible with the different GPR systems used, through an infinite sediment layer was estimated to be 90, 150 and 200 ns for the 800, 500 and 200 MHz systems, respectively. This indicated that the ice pockets could potentially be detected down to ~6, 9 and 13 m, respectively.

The test site was an area of buried ground ice covered by 2–3 m of sediments (see Fig. 9). The annual mean temperature in the area is −6.3°C and the permafrost in the area is believed to go down to 150 m. The active layer is estimated to be 2 m. The measurements were done in April before melting had begun; therefore, the ground was totally frozen at the time the measurements were taken and can therefore be considered as an area of permafrost.

The very low losses make the site very suitable for testing very high-frequency GPR systems like the WISDOM radar. The area is also easy to access from the research station Ny-Alesund on Svalbard.

The subsurface on Mars is frozen ground and the permafrost depth is several hundred meters. There may be buried ground ice but there is great uncertainty in at what depth. The electromagnetic losses are expected to be low on Mars. The Uversbreen test site has been chosen because the sediments have very low loss and there is buried ground ice at a depth that the WISDOM instruments can detect.

The data was collected to try out the feasibility to use the area as a test bed for testing the WISDOM radar prototype for the ExoMars mission.

The WISDOM-GPR is a gated step-frequency (SF) GPR operating in the frequency band 0.5–3 GHz. The prototype system can be run in either SF or FMCW modes and both modes can be run either CW or gated (Hamran et al., 2008). The WISDOM instrument is one of the instruments that have been selected to be part of the Pasteur payload of the ESA ExoMars mission (Hamran et al., 2007a, b, 2008). The Pasteur payload consists of three sets of instruments: the Panoramic instruments (a wide-angle camera, an infrared spectrometer and the radar WISDOM) that will perform large-scale scientific investigations at the rover location; the contact instruments mounted on the Rover robotic arm that will be used for cm-scale investigations of outcrops, rocks, soils and the analytical laboratory instruments that will analyze samples obtained by the subsurface drill (up to the depth of 2 m) on board the rover. The main scientific objectives for the

Fig. 10. The GPR set-up deployed in the measurement campaign.

Pasteur payload on board the mission rover are to search for traces of past and present life on Mars and to characterize the shallow subsurface. The exploration of the subsurface of the planet is essential since chances that life has survived on Mars increase with increasing burial depth.

The ground penetrating radar, WISDOM onboard the rover permits to obtain information about the subsurface before drilling. The WISDOM instrument objective is the exploration of the first ~3 m of the soil with a very high-range resolution in accordance with the objectives and expected capabilities of the drill exploration. It will allow the characterization of the subsurface environment through the detection of electromagnetic permittivity contrasts as a function of depth along the rover path. WISDOM will help the identification of sedimentary layers where it is most likely that organic molecules may be well preserved and shall thus support the search for subsurface signs of past life at the rover sites. In addition, the information collected with WISDOM nearby the observed outcrops will be used to drill at locations where the first bedrock layer is within the drill reach.

In this paper, preliminary GPR measurements were done with a Mala impulse radar system using 500 and 800 MHz with shielded antennas (see Fig. 10). For the 800 MHz antenna, the center frequency is 750 MHz and the −10 dB spectrum is from 450–1050 MHz; the bandwidth was estimated directly from the GPR data. In such a way, MALA-GPR covers the lower part of the spectrum to the WISDOM radar. Thus, the results from the 800 MHz should therefore give an indication on how the WISDOM radar should perform on this site.

The measurements were carried out in time-domain and thus the pre-processing strategy above described is exploited to achieve the inversion data in the frequency domain.

We assumed in the inversion procedure a value of the model relative dielectric permittivity of the soil equal to 5.76; this value was determined by using reflecting hyperbolas at the sediment/ice interface and agrees with the above said estimated electromagnetic velocity. No accurate indication of the conductivity soil was inferred by the measurements so that its value in the inversion scheme was assumed on the basis of the literature.

Some profiles, collected with the 500 and 800 MHz antenna, were processed by exploiting microwave tomographic approach. Here, for sake of brevity we report only few of the achieved reconstruction results.

The first test case refers to measurement collected by the 500 MHz antenna; the parameters adopted in the inversion and the measurement configuration are reported in Table 3. In particular, we assume an investigation domain of horizontal extent equal to 5 m and with extent along the depth ranging from 0.1 to 6.1 m. This means that, the final reconstruction results depicted in the following figures are achieved by the following strategy. First, we performed the single tomographic reconstruction for sub-domains of horizontal extent equal to 5 m and finally we superpose these tomograpic images to achieve the final result for the vertical profile.

Here, we report the reconstruction results for the scan profile 33 (210 m long). In particular, we report the reconstruction results of the region ranging from 120 to 140 m and 150 to 170 m compared to the raw data on which only an automatic gain control in applied (Figs. 11–14). The tomographic reconstruction results allow us to point out the presence, the location and the extent of the layers.

In the case of 500 MHz antenna, by the comparison between the tomographic reconstruction and the radar data we can gain the following conclusions. First the tomographic approach was able to retrieve the main features of the investigated scene, i.e, the location and the geometry of the buried interfaces. Furthermore,

Table 3
Parameters for the experimental data at 500 MHz.

Parameter	Value
Model relative dielectric permittivity of the soil	5.76
Model conductivity of the soil	0.001 S/m
Spatial step of the measurements	0.1 m
Measurement domain	5 m (51 points spaced by 0.1 m)
Frequency band	100–700 MHz
Frequency step	10 MHz (61 freq. exploited in the inversion)
Investigation domain	5 m (horizontal) × (0.1–6.1) m depth

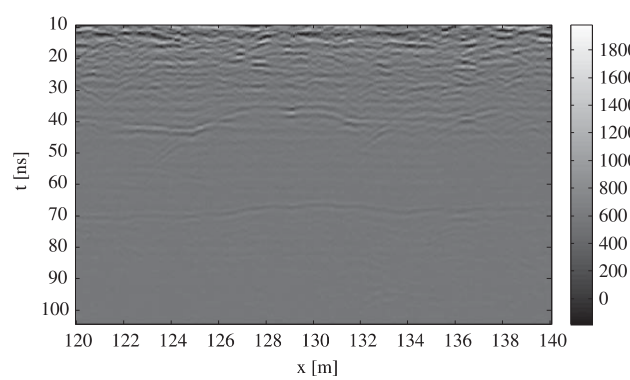

Fig. 11. 500 MHZ collected profile 33–120 to 140 m: time-domain data where an automatic gain is applied.

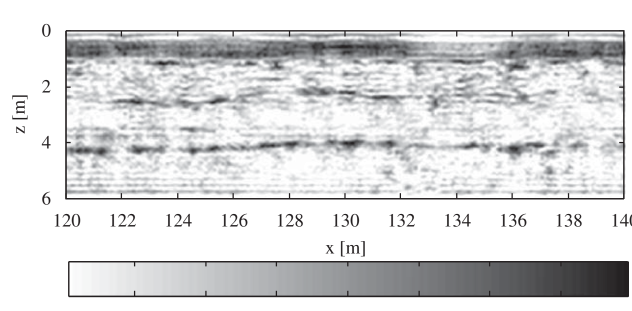

Fig. 12. 500 MHZ collected profile 33–120 to 140 m: modulus of the contrast function.

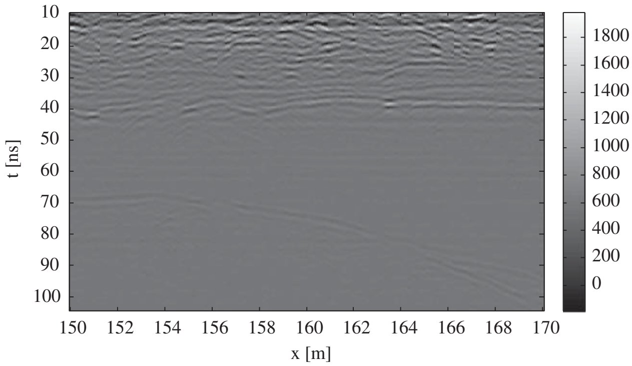

Fig. 13. 500 MHZ collected profile 33–150 to 170 m: time-domain data where an automatic gain is applied.

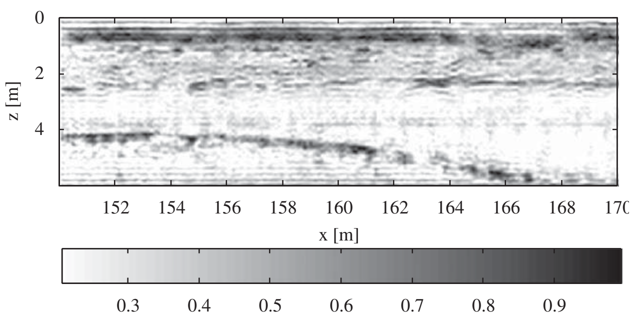

Fig. 14. 500 MHZ collected profile 33–150 to 170 m: modulus of the contrast function.

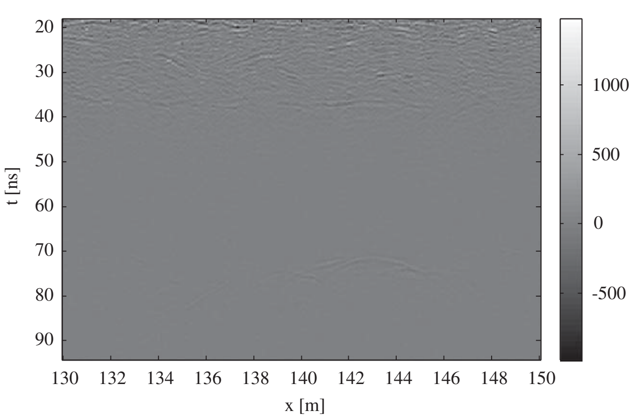

Fig. 15. 800 MHZ collected profile 27–130 to 150 m: time-domain data where an automatic gain is applied.

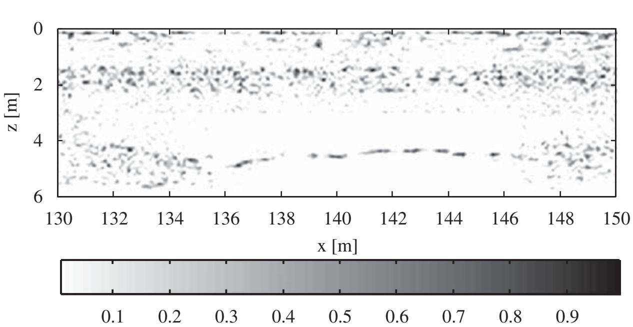

Fig. 16. 800 MHZ collected profile 27–130 to 150 m: modulus of the contrast function.

Table 4
Parameters for the experimental data at 800 MHz.

Parameter	Value
Model relative dielectric permittivity of the soil	5.76
Model conductivity of the soil	0.001 S/m
Spatial step of the measurements	0.1 m
Measurement domain	5 m (51 points spaced by 0.1 m)
Frequency band	100–1300 MHz
Frequency step	20 MHz (61 freq. exploited in the inversion)
Investigation domain	5 m (horizontal) × (0.1–6.1) m depth

the tomographic approach is able to give more focussed and clearer reconstruction of localized objects both in sediment and ice layers.

Furthermore, we have considered a scan profile (the profile 27) collected by a 800 MHz antenna. The comparison between the raw data and the reconstruction result of the region ranging from 130 to 150 m is shown by Figs. 15 and 16. For such a reconstruction result we have adopted the same strategy described above and the parameters adopted in the inversion for the reference scenario and the measurement configuration are reported in Table 4. As can be seen the tomographic reconstruction image show a better resolution, compared to previous cases, due to the increased extent of the frequency band exploited in the inversion that now ranges from 100 to 1300 MHz compared to the one exploited for the 500 MHz antenna (100–700 MHz).

Also in the case of 800 MHz antenna, the tomographic approach was able to give information on the location and the geometry of the two buried interfaces; such an information is retrieved in a clearer way for the deeper interface. In particular, the tomographic reconstruction of the interfaces appeared as a collection of localised objects. Finally, similarly to the case of the 500 MHz antenna, the tomographic approach exhibited good performances in focusing localised objects in the layers.

4. Conclusions

In this paper we have presented a novel processing algorithm for GPR data. The approach is based on microwave tomography and faces an inverse scattering algorithm with the aim of determining the electromagnetic properties of the buried objects starting from GPR measurements.

The feasibility of the microwave tomographic approach has been shown first with synthetic data and after with experimental survey in a scenario resembling the Mars conditions and that will be exploited as test bed for the WISDOM prototypical radar.

In particular, the synthetic and real test cases have pointed out how the tomographic approach allows to achieve reconstruction results that in some cases appear more easily interpretable compared to the raw data.

As future developments, we will address two topics. The first one is concerned with the experimental validation of the approach by means of the measurements collected by the WISDOM radar. The second one concerns the possibility to achieve 3D representation of the investigated scene.

References

Alberti, G., Dinardo, S., Mattei, S., Papa, C., Santovito, M.R., 2007. SHARAD radar signal processing technique. In: Proceedings of the forth International Workshop on Advanced Ground Penetrating Radar. Napoli, Italy, pp. 261–264.

Bertero, M., Boccacci, P., 1998. Introduction to Inverse Problems in Imaging. Institute of Physics Publishing, Bristol and Philadelphia.

Cerreti, A., Vannaroni, G., Del Vento, D., Pettinelli, E., 2007. Electromagnetic measurements on Martian soil analogs: implications for MARSIS and SHARAD radars in detecting subsoil water. Journal of Planetary and Space Sciences 55, 193–202.
Ciarletti, V., Corbel, C., Dolon, F., LeGall, A., Ney, R., Berthelier, J.J., Hamran, S.E., Plettemeier, D., the EISS Team, 2007. The EISS GPR on the ExoMars mission: deep soundings of the Martian subsurface. In: Proceedings of EMSEC 2007, Noordwijk.
Clifford, S.M., 1993. A model for the hydrologic and climatic behavior of water on Mars. Journal of Geophysical Research 98, 10973–11016.
Clifford, S.M., Parker, T.J., 2001. The evolution of the Martian hydrosphere: implications for the fate of a primordial ocean and the current state of the Northern plains. Icarus 154 (N1), 40–79.
Clifford, S., Heggy, E., Ciarletti, V, Le Gall, A., Kofman, W., Herique, A., 2007. A collaborative study of the use of multi-frequency GPR and other field and laboratory investigations of Mars analog environments. In: Proceedings of the second International Workshop—Exploring Mars and its Earth Analogues, Trento, Italy.
Daniels, D., 2004. Ground Penetrating Radar, 2nd Ed. IEE Press, London, UK.
Feldman, W.C., et al., 2002. Global distribution of neutrons from Mars: results from Mars Odissey. Science 297, 75–78.
Giannopoulos, A., 2003. GprMax2D V 1.5 (Electromagnetic simulator for Ground Probing Radar, the software is available at www.gprmax.org).
Hamran, S.E., Ciarletti, V., Corbel, C., Plettemeier, D., Øyan, M.J., Berger, T., Hanssen, L., 2007a. The WISDOM GPR on the ExoMars Mission. In: Proceedings of EMSEC 2007, Noordwijk.
Hamran, S.E., Berger, T., Hanssen, L., Øyan, M.J., Ciarletti, V., Corbel, C., Plettemeier, D., 2007b. A prototype for the WISDOM GPR on the ExoMars mission. In: Proceedings of the forth International Workshop on Advanced Ground Penetrating Radar. Napoli, Italy.
Hamran, S.-E., Ciarletti, V., Corbel, C., Plettemeier, D., Øyan, M. J., Berger, T., Hanssen1, L., 2008. The WISDOM Shallow Sounding GPR on the ExoMars Mission. In: Proceedings of the twelfth International Conference on Ground Penetrating Radar, June 16–19, 2008, Birmingham, UK.
Harrington, R.F., 1961. Time-Harmonic Electromagnetic Fields. Mc Graw Hill.
Leone, G., Soldovieri, F., 2003. Analysis of the distorted Born approximation for subsurface reconstruction: truncation and uncertainties effect. IEEE Transaction on Geoscience and Remote Sensing 41, 66–74.
Leighton, R.L., Murray, B.C., 1966. Behaviour of carbon dioxide and other volatiles on Mars. Science 153, 136–144.
Leuschen, C., Clifford, S., Gogineni, P., 2003a. Simulation of a surface-penetrating radar for Mars exploration. Journal of Geophysical Research 108, 16-1–16.14.
Leuschen, C., Kanagaratnam, P., Yoshikawa, K., Arcone, S., Gogineni, P., 2003b. Design and field experiments of a ground-penetrating radar for Mars exploration. Journal of Geophysical Research 108, 15-1–15.12.
Malin, M.C., Edgett, K.S., 2000. Evidence for recent groundwater seepage and surface runoff on Mars. Science 288, 2330–2335.
Meincke, P., 2001. Linear GPR inversion for lossy soil and a planar air-soil interface. IEEE Transactions on Geoscience and Remote Sensing 39, 2713–2721.
Mitrofanov, I., et al., 2002. Maps of subsurface hydrogen from the high energy neutron detector, Mars Odyssey. Science 297, 78–81.
Ori, G.G., Ogliani, F., 1996. Potentiality of the ground penetrating radar for the analysis of the stratigraphy and sedimentology of Mars. Journal of Planetary and Space Sciences 44, 1303–1315.
Paige, D.A., 1992. The thermal stability of near-surface ground ice on Mars. Nature 356, 43–45.
Persico, R., Soldovieri, F., 2004. Effects of uncertainty on background permittivity in one dimensional linear inverse scattering. Journal of Optical Society of America Part A 21, 2334–2343.
Persico, R., Bernini, R., Soldovieri, F., 2005. The role of the measurement configuration in inverse scattering from buried objects under the Born approximation. IEEE Transactions on Antennas and Propagation 53, 1875–1887.
Pettinelli, E., Vannaroni, G., Cereti, A., Paolucci, F., Della Monica, G., Storini, M., Bella, F., 2003. Frequency and time domain permittivity measurements on solid CO_2 and solid CO_2-soil mixtures as Martian soil simulants. Journal of Geophysical Research 108 (E4), 8029.
Pettinelli, E., Di Matteo, A., Soldovieri, F., Redman, D.J., Annan, A.P., 2008. GPR response from a buried plastic pipe filled with salty water: an experimental study. In: Procedings of the twelfth International Conference on Ground Penetrating Radar, June 16–19, 2008, Birmingham, UK
Picardi, G., et al., 2007. MARSIS data inversion approach: preliminary results. In: Proceedings of EMSEC 2007. Noordwijk.
Plaut, J.J., Picardi, G., Seu, R., Philips, R.J., the MARSIS and SHARAD Teams, 2007. Radar sounding of the polar regions of Marsis with SHARAD and MARSIS. In: Proceedings of EMSEC 2007. Noordwijk.
Safaeinili, A., Orosei, R., Philips, R., Plaut, J., Doubleday, K., Gim, Y., Campbell, B., Seu, R., 2007. Characterization of Radar transparent deposits in the southern and eastern Elysium region of Mars. In: Proceedings of EMSEC 2007. Noordwijk.
Slaney, M., Kak, A.C., Larsen, L.E., 1984. Limitations of imaging with first order diffraction tomography. IEEE Transactions on Microwave Theory and Techniques 32, 860–874.
Soldovieri, F., Hugenschmidt, J., Persico, R., Leone, G., 2007. A linear inverse scattering algorithm for realistic GPR applications. Near Surface Geophysics 5 (1), 29–41.
Solimene, R., Soldovieri, F., Prisco, G., Pierri, R., 2007. Three-dimensional microwave tomography by a 2-D slice-based reconstruction algorithm. IEEE Geoscience and Remote Sensing Letters 4, 556–560.
Steele, A., Amundsen, H.E.F., on Behalf of the AMASE 07 team, 2007. An overview of the Arctic Mars Analogue Svalbard Expedition 2007. Geophysical Research Abstracts. European Geosciences Union 2007, Vol. 9, pp. 11357.
Stolt, H., 1978. Migration by Fourier transform. Geophysics 43, 23–48.
Vannaroni, G., Pettinelli, E., Ottonello, C., Cerreti, A., Della Monica, G., Del Vento, D., Di Lellis, A.M., Di Maio, R., Filippini, R., Galli, A., Menghini, A., Orosei, R., Orsini, S., Pagnan, S., Paolucci, F., Pisani, A.R., Schettini, G., Storini, M., Tacconi, G., 2004. MUSES: Multi-sensor soil electromagnetic sounding.